Ion attachment rates and collection forces on dust particles in a plasma sheath with finite ion inertia and mobility

Toshisato Ono, Uwe R. Kortshagen,* and Christopher J. Hogan, Jr.†
Department of Mechanical Engineering, University of Minnesota, Minneapolis, Minnesota 55455, USA

(Received 30 August 2020; revised 15 November 2020; accepted 7 December 2020; published 31 December 2020; corrected 4 May 2021)

Ion attachment and ion drag to dust particles near the edge of a nonthermal plasma sheath are of interest to better understand how particles become trapped in such sheath regions. While electron-particle collisions in plasmas and sheaths can often be described by orbital motion limited theory, quantification of ion transport about dust particles in collisional sheath regions requires a distinct modeling approach. In this work, the dimensionless ion attachment coefficients and dimensionless collection forces on negatively charged particles are calculated using ion trajectory models accounting for an external electric field in a collisional sheath, ion inertia, and finite ion mobility. By considering both ion inertia and finite ion mobility, results apply for ion transport from the fully collisional regime into a regime of intermediate collisionality. Ion collection forces are calculated in two related limits; first, the nondissipative limit, wherein the dimensionless collection force function coincides with the dimensionless attachment coefficient (anticipated in the collisionless regime), and second, a dissipative limit, wherein neutral gas collisions dissipate ion momentum, which strongly affects the resulting collection force (anticipated in the fully collisional regime). We show that ion motion about a charged particle can be parametrized by the ion Stokes number, which is the ratio of ion inertia to gas resistance to motion and dimensionless electric field strength (the external field strength normalized by the electric field at the particle surface). At intermediate Stokes numbers (10^1–10^2), ions adopt trajectories that are extremely sensitive to the initial ion-particle impact parameter. Plots of the resulting collision angle at fixed Stokes number and dimensionless field strength as a function of impact parameter contain multiple discontinuities. Nonetheless, we obtain smooth curves for the ion attachment rates and collection forces in both the nondissipative and fully dissipative limits. Increasing the ion Stokes number is found to significantly decrease the dimensionless ion attachment coefficients and ion collection forces in comparison to coefficients evaluated with expressions derived in the fully collisional limit. In all instances, including the dissipative limit, we find the ion collection force acts in the direction of ion migration. Neural network fits are utilized to parametrize the resulting attachment coefficients and ion collection forces, and we apply these fits to examine the charge levels on 1-μm radius particles in external fields in the 3×10^2–3×10^3 V m^{-1} range and pressures in the 5×10^{-1}–5×10^1 Torr (66.7–6667 Pa) range. We find the charge level is strongly sensitive to both field strength and pressure in the plasma sheath, ranging from 2×10^2 to 2×10^3 over the conditions examined. Calculations are also used to demonstrate that the ion collection force can be sufficiently strong to trap particles not only close to the bottom electrode of a parallel-plate reactor, but also close to the top electrode, with a critical ion density required for trapping.

DOI: 10.1103/PhysRevE.102.063212

I. INTRODUCTION

The sheath region near the electrodes of nonthermal, parallel plate plasma reactors are characterized by a large time-averaged electric field directed towards the electrodes, corresponding to high ion migration velocities towards the electrodes, reduced ion densities, and further reduced electron densities in comparison to the plasma volume [1–3]. Interestingly, in particle-laden, dusty systems, particles invariably become trapped in this sheath region [4–12]. Particles are negatively charged both in the plasma volume and within the sheath region, and trapping is facilitated by a combination of electrostatic forces away from the electrodes, gravitational forces, and ion drag forces in the direction of net ion migration. The charging and forces on dust particles near the edge of the plasma sheath are hence of interest in studies of dusty space plasmas, fusion devices, and in plasma processing [13–20].

Nonetheless, the description of particle charge states and the magnitudes of forces on particles across a wide range of collisionality remains incomplete, particularly for collisional sheaths. Aside from their reduced density, electrons remain at high energy in the sheath, such that in most conditions, electron-particle collisions can be described by the orbital motion limited approach [21] that also applies in the plasma volume. However, ion attachment and ion momentum transfer to particles are less clearly described in plasma sheath regions. While ion attachment [22–25] and ion drag [14,19,20,26–32] have been studied extensively under conditions more relevant to the volume of a dusty plasma, the large field strengths in plasma sheaths can yield significantly higher ion velocities than are encountered in the plasma volume, and there is hence a need to develop ion-particle transport relationships relevant

*Corresponding author: korts001@umn.edu
†Corresponding author: hogan108@umn.edu

to plasma sheath regions, which has been largely studied in the collisionless limit with respect to particle-ion interactions [33–35].

In many regards, ion-particle interactions in collisional sheath regions resemble the interactions between two disparately sized and oppositely charged aerosol particles in an external field, which have different migration velocities [36,37]. In such systems, trajectory calculations find utility in determining transport rates and can be applied to examine collision dynamics. Here, we adopt such trajectory calculations to determine ion-particle attachment rates (defining particle charging rates) and ion collection forces (the contribution to ion drag from direct collisions) for particles trapped in the sheath region of a plasma. The resulting relationships apply in conditions wherein plasma species are dilute, the particle is negatively charged, plasma screening effects are negligible, and the electric field strength leads to ion velocities above thermal velocities. We believe the results are particularly useful in evaluating ion-particle collisions and the ion collection force in instances where ion motion about a particle in collisional sheaths is strongly influenced by ion-neutral collisions. Following from approaches applied in aerosol science, we demonstrate that under these conditions, dimensionless transport rates can be defined in terms of a dimensionless representation of the external field strength and an ion Stokes number, quantifying ion inertia relative to frictional resistance to motion provided by neutral background gas. Fitting the dimensionless attachment rates and forces via a neural network, we compare the attachment coefficient derived for the sheath region to prior work analyzing attachment both in the presence of an ion-particle velocity difference [38] and in the plasma volume [25].

II. CALCULATION METHODS

A. Ion equations of motion

In developing relationships for ion transport rates to negatively charged particles in sheath regions, we make the simplifying approximations that (1) the initial thermal motion of ions is negligible in comparison to the electrostatically driven ion migration velocity and (2) ion and electron densities are sufficiently dilute to neglect electrostatic screening, i.e., ion motion can be monitored about a charged particle neglecting ion-ion and ion-electron interactions. Figure 1 displays a schematic diagram of ion trajectories about a negatively charged particle, applying these assumptions. Each ion, at a prescribed impact parameter from the particle center (b, aligned with the y axis for simplicity), initially has x-direction velocity $V_0 = K(\frac{E}{N})E_x$, where E_x is the electric field strength in the sheath region and $K(\frac{E}{N})$ is the ion's mobility, which depends upon the field strength to gas density ratio ($\frac{E}{N}$) [39]. Considering finite ion inertia and mobility, as well as a negatively charged particle interacting Coulombically with the ion, the resulting equations of motion for the ion are

$$m_i\frac{d^2x}{dt^2} = -eE_x - \frac{qex}{4\pi\varepsilon_0(x^2+y^2)^{3/2}} - \frac{e}{K\left(\frac{E}{N}\right)}\frac{dx}{dt}, \quad (1a)$$

$$m_i\frac{d^2y}{dt^2} = -\frac{qey}{4\pi\varepsilon_0(x^2+y^2)^{3/2}} - \frac{e}{K\left(\frac{E}{N}\right)}\frac{dy}{dt}, \quad (1b)$$

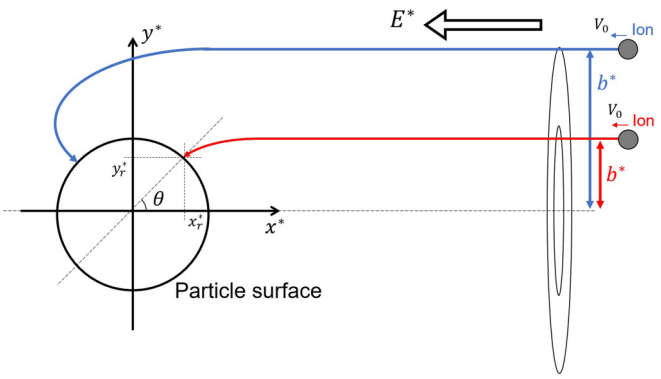

FIG. 1. Schematic diagram of the ion trajectory calculations. Two initial impact parameters, b, are shown; the smaller results in an ion impinging upon the front face of the particle, while the larger impact parameter leads to an impinging ion on the back face of the particle. Ions impinge upon particles at locations (x_r^*, y_r^*), with $\theta = \tan\frac{x_r^*}{y_r^*}$.

where m_i is the ion mass, e is the unit electron charge, ε_0 is the permittivity of free space, q is the absolute integer charge on the particle (a positive value). We assume E_x is a constant in the vicinity of the particle with a negligible gradient. In actual dusty plasma where particles are trapped in an electrode sheath, E_x is not constant but increases towards the electrode surface [40], and an appreciably large gradient relative to the particle size would require corrections to the present analysis. Introducing the length scale normalizations $x^* = \frac{x}{a_p}$ and $y^* = \frac{y}{a_p}$, where a_p is the particle radius, and the time-scale normalization $\tau = \frac{tK_0E_x}{a_p}$, yields the following dimensionless equations of motion:

$$\mathrm{St}\frac{d^2x^*}{d\tau^2} = -1 - \frac{x^*}{E^*(x^{*2}+y^{*2})^{3/2}} - \frac{1}{f\left(\frac{E}{N}\right)}\frac{dx^*}{d\tau}, \quad (2a)$$

$$\mathrm{St}\frac{d^2y^*}{d\tau^2} = -\frac{y^*}{E^*(x^{*2}+y^{*2})^{3/2}} - \frac{1}{f\left(\frac{E}{N}\right)}\frac{dy^*}{d\tau}, \quad (2b)$$

where $f(\frac{E}{N}) = [K(\frac{E}{N})/K_0]$ is a dimensionless mobility function normalizing the mobility by the ion's mobility at a field strength E_x (K_0), E^* is the dimensionless field strength, and St is the Stokes number [41,42]. We assume $f(\frac{E}{N}) = 1$ for simplicity here, but note the calculation procedure can be modified to account for the variation in mobility with field strength [43]. E^* and St are given by the equations

$$E^* = \frac{4\pi\varepsilon_0E_xa_p^2}{qe}, \quad (3a)$$

$$\mathrm{St} = \frac{K_0^2E_xm_i}{ea_p}. \quad (3b)$$

The Stokes number, quantifying the influence of ion inertia on the resulting ion trajectories in comparison to the resistance to a motion brought about by collisions with background gas, is proportional to the product of the ion Mach number (Ma, which itself is proportional to the ion migration velocity to ion mean thermal speed ratio) and mass-transfer (diffusive) Knudsen number (Kn, a ratio of ion diffusion coefficient to a

product of particle radius and ion mean thermal speed). This yields St $\propto$ KnMa, as discussed in prior studies of aerosol transport [44,45], though with Ma represented as a translational energy to thermal energy ratio proportional to Ma^2. Because of this proportionality Eqs. (2a) and (2b) do describe ion motion across a wide range of collisionality; in the St $\to 0$ limit Eqs. (2a) and (2b) converge to the system described by Khrapak *et al* [46] and commented on by Hutchinson [47], while in the St $\to \infty$ limit the last term in Eqs. (2a) and (2b) is negligibly small, and ballistic or collisionless kinetics describe ion-particle transfer rates. Interestingly, the equations of motion implemented show that increasing the Mach number has the same effect as reducing the pressure in the system. Therefore, for ion migration about a charged particle in the presence of an external electric field, the terms fully inertial and collisionless, as well as inertialess and fully collisional, coincide with one another. We remark that degree of collisionality in this work refers to the extent to which ion-neutral collisions affect ion motion about a particle, i.e., over the relevant length scale of ion-particle collisions, and strictly apply in instances where ion transport in the sheath region is fully collisional (leading to the assumption that the initial ion velocity is the product of its mobility and the field strength). We also note that although these equations enable approximation of ion motion on approach to a negatively charged particle, they only enable determination of ion mass and momentum transport rates to particles with particle size and charge known and in the dilute ion density limit, and we presently neglect motion of the particle induced by the approaching ion. For this reason, the simulations performed cannot be described as self-consistent [48] (i.e., particle charge needs to be determined through other means, as does the ion density and initial velocity). We also neglect the influence of charge exchange [49,50], wherein during ion migration, the positive charge is transferred to a neutral of significantly lower translational energy. In the fully collisional, inertialess limit, by definition, charge exchange has no influence on trajectories. We performed preliminary trajectory calculations accounting for charge exchange; these revealed that charge exchange could occur (using estimates for the charge exchange cross section from prior studies) for ions in trajectory calculations; however, such reactions would not influence the resulting final impact location and impact velocity unless the charge exchange cross section greatly exceeded values determined from prior experiments and computations.

B. Attachment rates and collection forces

For $E^* = 10^{-4}$–10^{1} and St = 0–500, as well as selected instances in the $E^* = 10^{-5}$–10^{-4} range (for subsequent neural network fitting), we solve Eqs. (2a) and (2b) for variable initial impact parameters (i.e., y^* locations) to determine the critical impact parameter (b_c^*) below which collision occurs and above which ions do not collide with particles. Calculations are performed using the Störmer-Verlet method, described in the Appendix, with initial conditions of $x^*(0) = 10^4$, $\frac{dx^*}{d\tau}(0) = 1$, and with an empirically tuned moving time step based on the criterion $d\tau = (\frac{2\times 10^4}{x^{*2}+y^{*2}} + 0.1)^{-1}$. In systems of Coulombically attracting inertial particles in a shear field [35], trajectories leading to noncollision for $y^* < b_c^*$ have been observed. However, we do not find similar instances here and for all instances where, $y^* < b_c^*$, collision occurs. The ion attachment coefficient α_i is used to define the rate at which ions impinge upon and transfer positive charge to particles; the charging rate is the product of ion attachment coefficient and ion concentration. Because collision occurs for all $y^* < b_c^*$, the dimensionless ion attachment coefficient (α_i^*) can be directly calculated from trajectory calculation results as

$$\alpha_i^* = \frac{\alpha_i}{\pi K\left(\frac{E}{N}\right) E_x a_p^2} = \frac{2\pi n_i \int_0^{b_c} y_i dy_i}{\pi n_i K\left(\frac{E}{N}\right) E_x a_p^2} = b_c^{*2}, \tag{4}$$

where y_i denotes the initial y location of an ion. Assuming that upon collision, ions yield their full momentum to particles (the diffuse model of momentum transfer), then the dimensionless ion collection force (F_i^*) in the direction of ion migration can be determined as

$$F_i^* = \frac{F_i}{\pi n_i m_i K^2\left(\frac{E}{N}\right) E_x^2 a_p^2} = \frac{2\pi n_i K\left(\frac{E}{N}\right) E_x \int_0^{b_c} \Delta p(y_i) y_i dy_i}{\pi n_i m_i K^2\left(\frac{E}{N}\right) E_x^2 a_p^2}$$
$$= 2\int_0^{b_c^*} \Delta v^*(y_i^*) y_i^* dy_i^*, \tag{5}$$

where F_i is the dimensional ion collection force, n_i is the ion density in the sheath region, $\Delta p(y_i)$ is the change in momentum brought about by impingement of an ion initially at y location y_i, and $\Delta v^*(y_i^*)$ is the dimensionless ion momentum transfer to the particle per unit ion mass. Calculation of $\Delta v^*(y_i^*)$ requires application of conservation of momentum during each trajectory where collision occurs. In doing so, we examine two limits for $\Delta v^*(y_i^*)$. First, we consider a scenario where the ion and particle minimally exchange momentum with the neutral gas on close approach, independent of input E^* and St. In this "nondissipative" limit, which applies exactly when ion motion is fully collisionless (high Stokes number), momentum is fully conserved in the isolated ion-particle system, and $\Delta p(y_i) = m_i K(\frac{E}{N}) E_x$, hence $\Delta v^*(y_i^*) = 1$ for all y_i^*. This instance, therefore, leads to $F_i^* = b_c^{*2} = \alpha_i^*$, as is the case for the ion collection force derived in the fully collisionless limit previously [51]. Furthermore, with minimal influence of neutral gas, the orbiting force due to grazing collisions described and derived previously [27,51] is applicable, with the ion drag force the sum of the collection and orbiting forces.

In contrast, in a fully dissipative limit (applicable in the fully collisional, low Stokes number limit), neutral gas collisions are so prevalent such that grazing trajectories impart no momentum to the particle directly (though can by influencing neutral motion, i.e., via hydrodynamic interaction). Momentum exchange between the ion and particle only occurs at the point of collision, and the fully dissipative limit leads to $\Delta v^*(y_i^*) = v_{f,x}^*(y_i^*)$, the ion velocity in the direction of the electric field, at the point of collision, as a function of initial impact parameter. Therefore, in addition to tracking the critical impact parameter, at the point of collision, we track the ion velocity in the direction of the external field, denoted as $v_{f,x}^*$.

We subsequently report both α_i^*, the dimensionless attachment coefficient and dimensionless collection force in the nondissipative limit, and F_i^* from Eq. (5) applying the as-

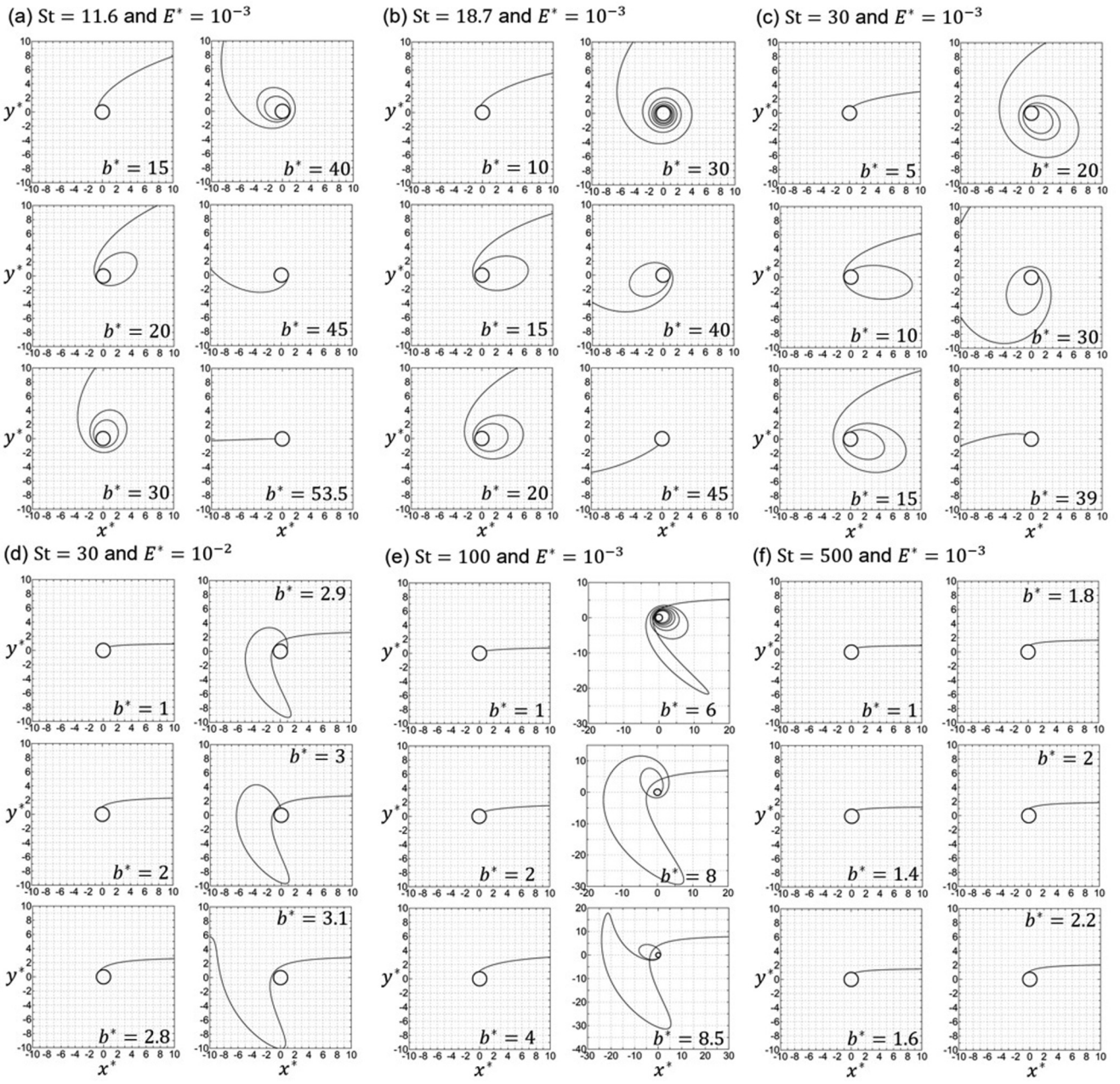

FIG. 2. Calculated ion trajectories for selected collision parameter b^*, E^*, and St > 10. Trajectories are centered on the region near to the particle.

sumptions of the fully dissipative system. Fully dissipative limit calculations are performed assuming immobile particles. Further clarification on the collection force, which falls intermediate to these two limits, would require additional calculation of the particle trajectory during approach by the ion, and is hence dependent on an appropriately defined particle Stokes number as well (as both particle inertia and neutral drag need to be considered).

The integrations required for Eqs. (5) in the fully dissipative limit were carried out similarly to the methods of Goudeli *et al.* [52]. Specifically analyzing $v^*_{f,x}$ as a function of St and b^* for a given dimensionless field strength, we first used linear interpolation with Delaunay triangulation [53] in between directly calculated conditions. Further smoothing of $v^*_{f,x}(b^*, \mathrm{St})$ was conducted using thin plate spline interpolation [54] prior to integration.

III. RESULTS AND DISCUSSION

A. Ion trajectories

Individual trajectory calculations result in ion path lines in the x-y plane and either collision or noncollision with the central particle for each prescribed St, E^*, and b^* input. Figure 2 depicts selected zoomed-in views of ion path lines at elevated Stokes number, with lower Stokes number trajectories noted in Fig. 3. At low Stokes numbers, ion trajectories reveal rather simple behavior. Below a particular Stokes number-dependent and dimensionless field strength-dependent impact parameter,

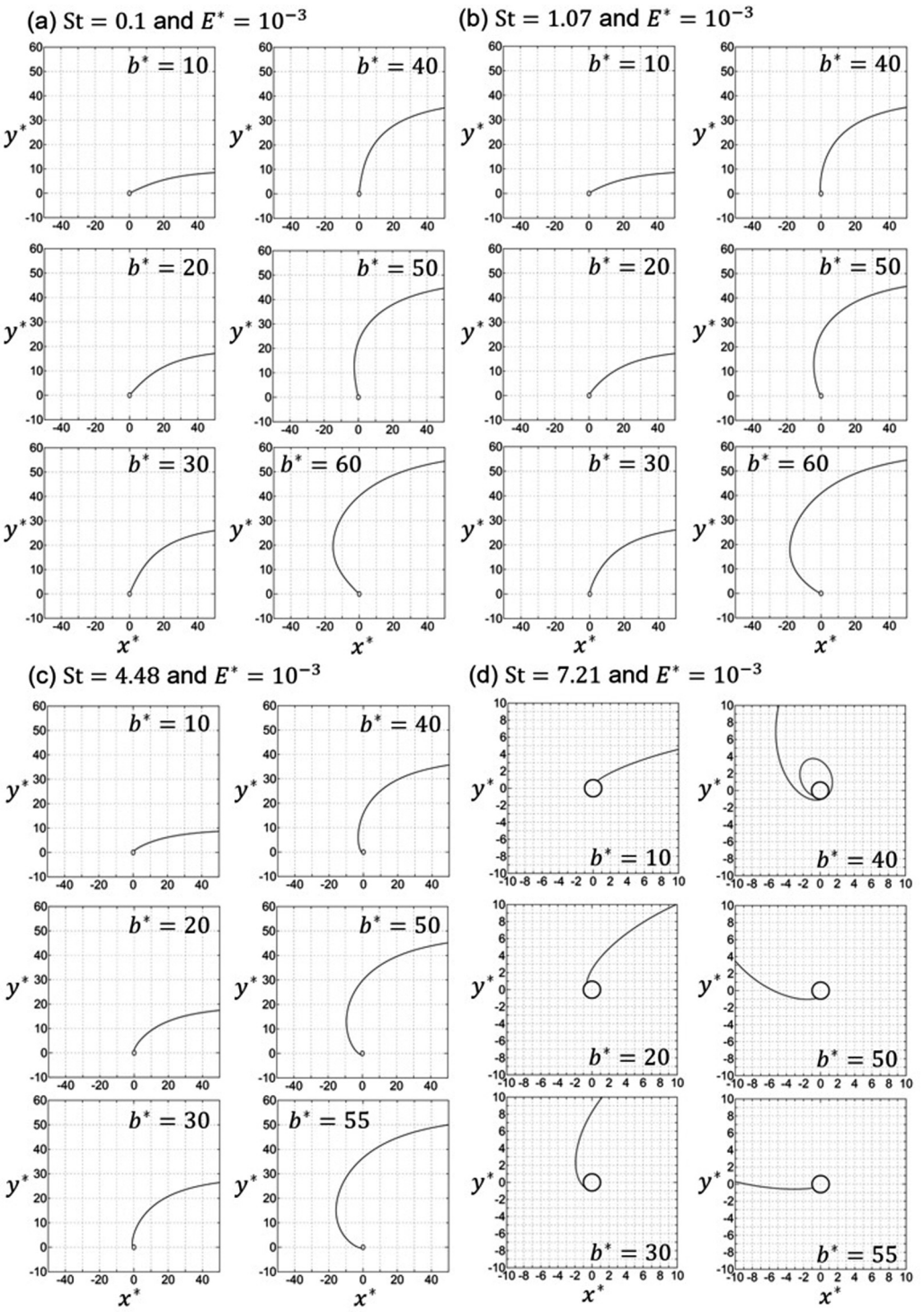

FIG. 3. Calculated ion trajectories for selected collision parameter b^*, E^*, and St < 10. Trajectories are centered on the region near to the particle.

ions collide on the front face, where θ, the collision angle, remains below 90°. For $E^* < 1$, within a narrow range of larger impact parameters, ions collide on the back face ($90^\circ < \theta < 180^\circ$). These scenarios are both depicted in Fig. 1 (red and blue ions, respectively). However, as has been observed in evaluations of trajectories of finite inertia charged dust grains in shear fields [42], significantly more complex ion trajectories are observed at intermediate Stokes number and lower energy ratio values (i.e., the scenarios depicted in Fig. 2). Specifically, as the impact parameter increases, elevated Stokes number ions can adopt (1) spiraling trajectories which completely orbit the particle a finite number of times prior to collision [Figs. 2(a)–2(c)], (2) trajectories wherein the ion passes far into the second quadrant of the computational domain before returning and colliding with the particle [lower right of Figs. 2(a)–2(e)], and (3) collision angles which

TABLE I. α_i^* for variable E^* and St, as determined by trajectory calculations.

E^*	St = 0.0	St = 0.1	St = 0.42	St = 1.07	St = 2.79	St = 4.49	St = 7.21	St = 11.6	St = 18.7	St = 30	St = 50	St = 100	St = 200	St = 500
0.0001	39832.1	39960.0	39840.1	39601.0	39047.3	38497.58	37632.12	36256.0	34077.2	30723.1	25312.8	14884.0	4225.00	42.250
0.000316	12622.5	12624.8	12561.9	12441.2	12145.8	11837.01	11365.69	10611.1	9446.29	7758.44	5343.61	1814.76	118.810	13.690
0.001	3999.9	3990.62	3955.81	3885.15	3718.12	3555.691	3286.78	2889.78	2323.43	1584.82	739.840	72.250	10.890	4.840
0.00316	1266.6	1258.66	1242.81	1200.01	1109.73	1016.324	878.988	689.222	447.005	205.496	39.690	7.290	4.000	2.310
0.01	400.278	396.404	386.113	364.408	314.665	266.607	202.125	123.599	50.802	9.057	4.840	2.890	1.960	1.346
0.0316	126.666	124.669	119.103	106.608	80.900	57.909	33.711	12.290	4.289	2.900	1.960	1.440	1.323	1.000
0.1	40.031	38.976	35.820	29.579	17.074	9.021	3.247	2.563	1.928	1.441	1.210	1.000	1.000	1.000
0.316	12.670	11.544	10.199	7.211	2.792	1.962	1.692	1.441	1.211	1.001	1.000	1.000	1.000	1.000
1	4.003	3.433	2.633	1.934	1.490	1.211	1.211	1.001	1.001	1.001	1.000	1.000	1.000	1.000
3.16	1.734	1.554	1.296	1.274	1.146	1.001	1.001	1.001	1.001	1.001	1.000	1.000	1.000	1.000
10	1.211	1.029	1.025	1.017	1.041	1.001	1.001	1.001	1.001	1.001	1.000	1.000	1.000	1.000

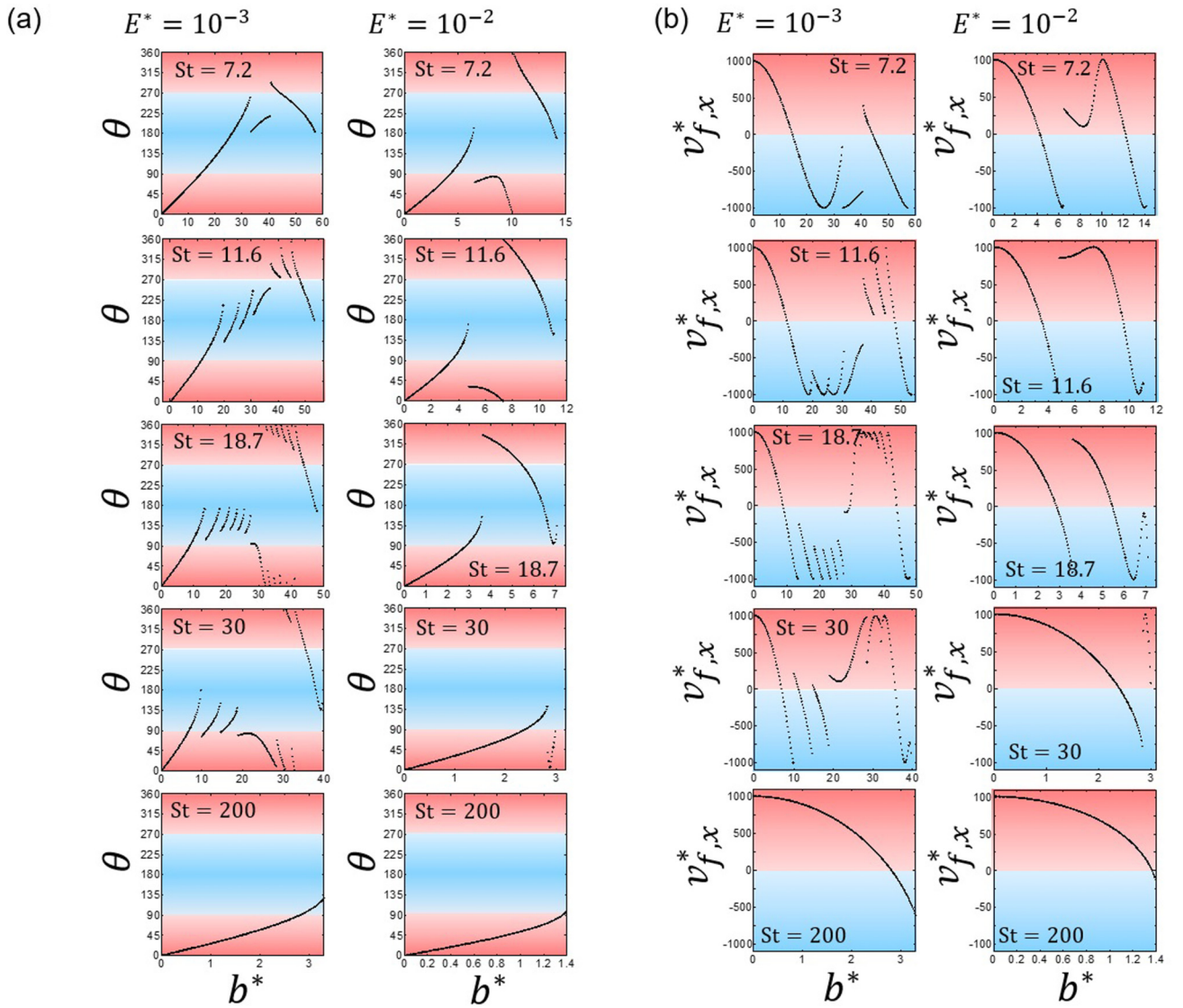

FIG. 4. The collision angle θ as a function of impact parameter b^* (a) and the collision velocity $v^*_{f,x}$ as a function of the impact parameter b^* (b). The red shading indicates ions imparting momentum in the direction of ion migration, while blue denotes ions imparting momentum opposing the direction of ion migration.

TABLE II. F_i^* in the fully dissipative limit for variable E^* and St, as determined by trajectory calculations.

$E*$	St = 0.0	St = 0.1	St = 0.42	St = 1.07	St = 2.79	St = 4.49	St = 7.21	St = 11.6	St = 18.7	St = 30	St = 50	St = 100	St = 200	St = 500
0.0001	53400	47500	34400	23700	25500	22200	41100	31400	41200	27600	29500	27100	23900	24072
0.000316	9504.0	8166.0	10600	10798.0	18179.0	15487.0	13900.0	20300.0	14351.0	14793.0	18157.0	13230.0	8686.4	5257.6
0.001	7310.0	7280.0	7290.0	7370.0	6710.0	7450.0	6980.0	6670.0	6610.0	4360.0	3407.5	2496.5	1580.5	1231.1
0.00316	1731.0	1726.0	1721.0	1740.0	1620.0	1810.0	1380.0	1450.0	953.00	984.00	509.55	436.04	370.04	295.04
0.01	565.34	411.00	410.00	402.00	404.00	359.00	310.00	319.00	242.00	153.00	124.54	105.15	90.36	76.27
0.0316	113.19	98.70	97.70	90.90	93.40	77.90	69.30	54.30	43.70	40.60	31.04	26.96	24.66	22.55
0.1	26.86	24.50	23.60	21.50	19.40	16.50	14.30	13.60	12.90	12.40	8.606	7.797	7.775	7.730
0.316	8.490	7.160	6.730	6.260	5.510	5.270	5.070	4.910	4.760	4.590	3.125	3.124	3.120	3.115
1	3.460	3.170	3.000	2.810	2.640	2.510	2.500	2.390	2.390	2.390	1.663	1.665	1.666	1.667
3.16	1.720	1.960	1.850	1.850	1.790	1.710	1.710	1.710	1.710	1.710	1.208	1.210	1.210	1.211
10	1.210	1.500	1.500	1.510	1.530	1.500	1.510	1.510	1.510	1.510	1.066	1.066	1.066	1.067

change discontinuously with small changes in impact parameter [Fig. 2(d)]. The consequence of type (3) trajectories are the plots in Fig. 4 of the collision angle as a function of impact parameter [Fig. 4(a)] and v_f^* as a function of impact parameter [Fig. 4(b)]. Red and blue shading are utilized to highlight whether the impinging ion collides moving parallel to (red) or against (blue) the direction of ion migration. For cases in the range $7.2 \leqslant \mathrm{St} \leqslant 30$ we find multiple discontinuities in both collision angle and collision velocity with changing impact parameter; in some instances (e.g., St = 18.7 and $E^* = 10^{-3}$) there are more than ten discontinuities in plots. We are not able to discern any systematic evolution of collision angle with Stokes number, although the number of discontinuities appears to be maximized for Stokes numbers from 10^0 to 10^1, as it tends to zero at low and high Stokes numbers, i.e., in the fully collisional (low Stokes number) and collisionless limits (high Stokes number).

B. Attachment coefficient and nondissipative collection force

Integration results are summarized in Tables I and II, which list α_i^*, and F_i^* in the fully dissipative limit, respectively. However, before directly calculating ion attachment coefficients utilizing critical impact parameters, we remark that in the fully collisional, $\mathrm{St} \to 0$ limit, the dimensionless attachment coefficient, and nondissipative collection force resulting from the applied equations of motion has the functional form [47]

$$\alpha_1^* = \frac{4}{E^*} \quad E^* \leqslant 1, \tag{6a}$$

$$\alpha_2^* = 1 + \frac{1}{E^{*2}} + \frac{2}{E^*} \quad E^* > 1. \tag{6b}$$

Equation (6a) coincides with the Langevin fully collisional ion-ion recombination coefficient [55]. In the Langevin approach, the attachment coefficient is evaluated in the absence of a net migration velocity for either of the colliding entities. Its recovery from the equations of motion neglecting ion inertia (originally by Maxwell [56]) demonstrates that the applied equations of motion and initial conditions still properly lead to the low Mach number attachment coefficient. Figure 5 displays plots of the dimensionless ion attachment coefficient from Eq. (4) as a function of the dimensionless electric field for $0 \leqslant \mathrm{St} \leqslant 500$. Curves corresponding to Eqs. (6a) and (6b) are also plotted. St = 0 calculations are in excellent agreement with Eqs. (6a) and (6b) in the low and high field limits, respectively, demonstrating the proper convergence of trajectory calculations results to analytical solutions. In contrast with the complex behavior of individual trajectories themselves, the ion attachment coefficients display systematic and clearly discernable dependencies on St and E^*. As Stokes number increases, greater deviations from Eqs. (6a) and (6b) are evident. More specifically, at infinite Stokes number, $\alpha_i^* \to 1$, and as Stokes number increases, α_i^* hence remains near 10° for increasingly low values of E^*. A consequence of this behavior is that the dimensionless attachment coefficient is strongly sensitive to Stokes number, e.g., for E^* near 3.16×10^{-3}, the attachment coefficient decreases by nearly three orders of magnitude as St varies from 1 to 500.

C. Fully dissipative collection force

In the fully dissipative limit, ion collection force calculations at fixed dimensionless field strength and Stokes number

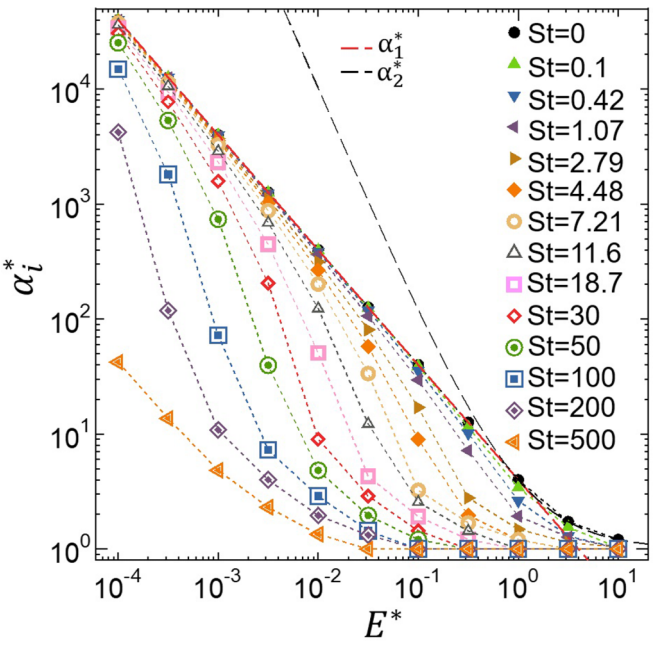

FIG. 5. Nondimensionalized ion attachment coefficient and nondissipative collection force as a function of dimensionless field strength.

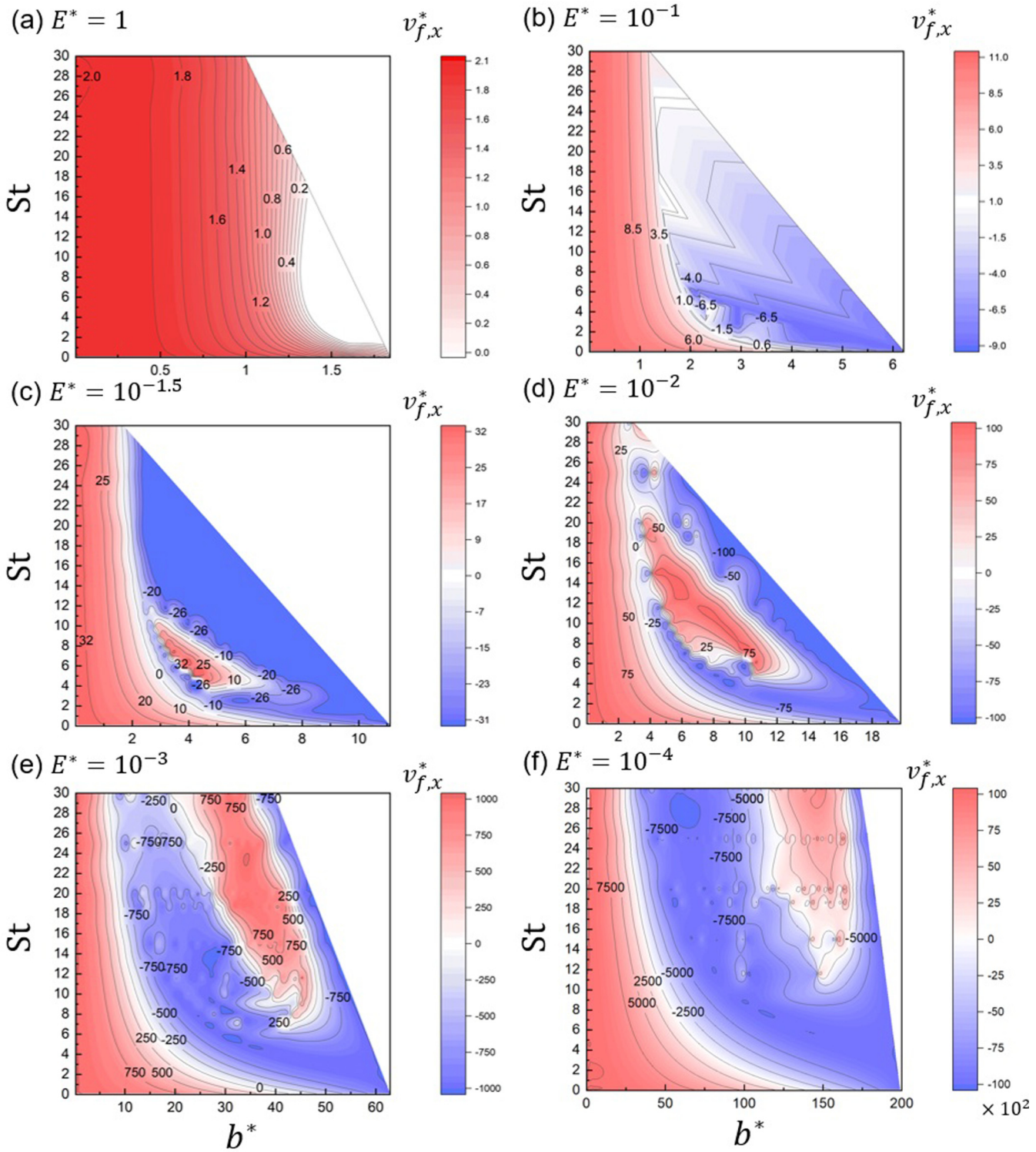

FIG. 6. Contour plots of the ion velocity in the x direction at collision as a function of both dimensionless impact parameter and Stokes number. Labels are provided to denote lines of constant impact velocity.

depend upon the impinging ion velocity as a function of impact parameter. Contour plots of the dimensionless velocity at impact in the direction of ion migration are provided in Fig. 6 for the range St = 0–30, where the independent variables are dimensionless impact parameter and Stokes number (integration to determine the ion drag force hence occurs over horizontal lines). At large values of the dimensionless field strength, ions never attain negative velocities at the point of collision, as ions only collide at collision angles below θ. However, as the dimensionless field strength drops below unity, ion collisions at $90^\circ < \theta < 270^\circ$ become possible, and at each Stokes number, there exists an impact parameter beyond which the ion velocity at impact switches from positive to negative. As Stokes number increases, the impact parameter

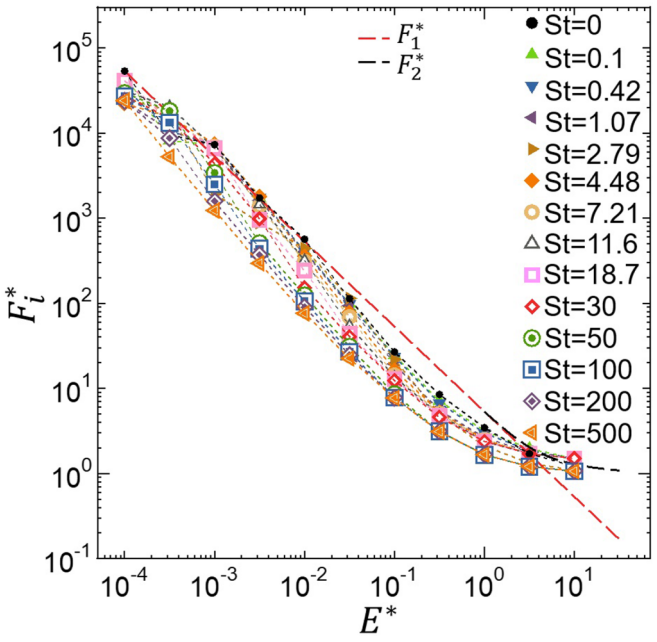

FIG. 7. Nondimensionalized ion collection force in the fully dissipative limit as a function of dimensionless field strength at selected Stokes numbers.

where the switch in the sign of impinging ion momentum transfer occurs becomes smaller. Interestingly, at intermediate Stokes numbers, low values of E^* ($< 10^{-1}$), and impact parameters beyond the initial "flip" to negative momentum transfer at collision, a second flip back to positive momentum transfer is observed at a larger impact parameter. Proceeding to further increase the impact parameter, this is followed by a third flip again to negative momentum transfer, and finally, an impact parameter is reached at which the ion does not collide with the particle. As this flipping behavior occurs in neither the inertialess nor fully inertial limits, it results in an "island" of positive ion drag contribution visible in the Fig. 6 contour plots for ions of elevated inertia and large impact parameter.

In the inertialess limit, the equations of motion yield the fully dissipative dimensionless ion collection force as [47]

$$F_1^* = \frac{16}{3E^*}, \quad E^* \leqslant 1 \tag{7a}$$

$$F_2^* = 1 + \frac{8}{3E^*} + \frac{2}{E^{*2}} - \frac{1}{3E^{*4}} E^* > 1. \tag{7b}$$

These functions yield positive ion drag values (in the direction of ion migration) for all values of E^*. In the fully inertial limit, with a constant electric field, $F_i^* = 1$, hence the force remains positive in the two limits of interest. However, because of ion impingement on the back face of the particle at elevated impact parameters, which contribute more heavily to the integrated ion drag, there is no guarantee that the ion drag force remains positive across all of St, E^* space. Integrated ion collection forces from Eq. (5) are plotted in Fig. 7. At small Stokes numbers, plots show reasonable agreement with Eqs. (7a) and (7b) in the low and high field strength limits, respectively. At the lowest field strength examined, the deviations evident with Eq. (7a) likely result from the need to interpolate and numerically integrate a function with multiple discontinuities. Immediately evident is that for all examined conditions, the net ion collection force on a particle remains positive [57]. Furthermore, similar to the ion attachment coefficient, deviations of the dimensionless collection force from the inertialess limit increase in magnitude with increasing Stokes number. At the same time, the fully dissipative collection force is found to be significantly less sensitive to Stokes number than the ion attachment coefficient; as St is varied from 0 to 500, for all examined E^* values the fully dissipative collection force varies by less than an order of magnitude. This is presumably because of the noted "islands" of positive collection force observed in the Fig. 6 contour plots; their existence maintains a net positive collection force in the intermediate Stokes number range.

D. Case studies

With dimensionless attachment coefficient and ion collection force expressions established, we compare results to those obtained in prior analyses of ion attachment with a net velocity difference between particle and ion [38] and ion attachment in the plasma bulk [25]. Comparison is made in the limit of large screening length relative to both the particle radius and the mean free path of the ions, where our results apply. We also apply the relationships developed here to make predictions of charge levels on microparticles, as well as the collection forces on microparticles in sheath regions of prescribed electric field strength. To facilitate all calculations, we developed a neural network that fits trajectory calculation results. The deep learning toolbox in MATLAB was utilized to obtain the neural networks, with inputs $\ln E^*$ and $\ln \mathrm{St}^*$ and outputs $\ln(\alpha_i^*/\alpha_i^*|_{\mathrm{St}=0})$ and $\ln(F_i^*/F_i^*|_{\mathrm{St}=0})$ (for the fully dissipative limit), where the subscript $\mathrm{St} = 0$ refers to the inertialess limiting expressions for the ion attachment coefficient and ion drag force, respectively. Fitting hence resulted in the expressions

$$\alpha_i^* = \alpha_i^*|_{\mathrm{St}=0} \exp(f[\ln(E^*), \ln(\mathrm{St}^*)]), \tag{8a}$$

$$F_i^* = F_i^*|_{\mathrm{St}=0} \exp(g[\ln(E^*), \ln(\mathrm{St}^*)]), \tag{8b}$$

where $f[\ln(E^*), \ln(\mathrm{St}^*)]$ and $g[\ln(E^*), \ln(\mathrm{St}^*)]$ are the neural network outputs. The networks each had 15 layers, and the Levenberg-Marquardt algorithm was used in training [58]. Comparisons of neural network predictions to the attachment coefficients and drag forces from trajectory calculations are displayed in Fig. 8, confirming that the neutral networks recover trajectory calculation results with high accuracy.

We first compare our results to the physical model developed and applied by Khrapak and colleagues [38] for ion attachment to a particle in the presence of a velocity difference between ions and particles, as would be encountered for trapped particles in a sheath region. They note that in the collisionless limit, the dimensionless attachment coefficient ($\alpha_{K,WC}^*$) can be expressed as (using the notation in

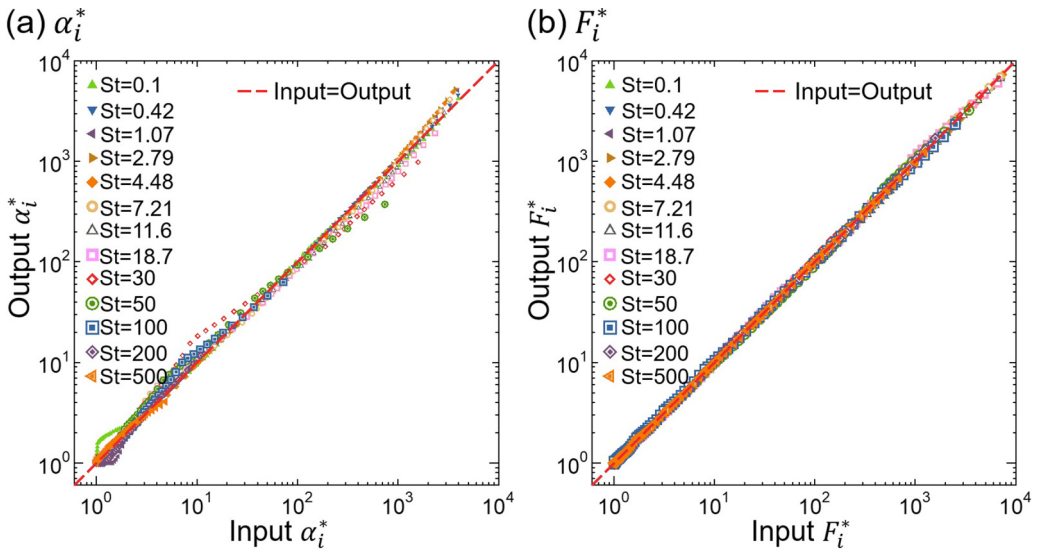

FIG. 8. A comparison between trajectory-calculated (input) and neural network output values for the dimensionless ion attachment coefficient and nondissipative collection force (a) and the dimensionless ion collection force in the fully dissipative limit (b).

this work):

$$\alpha^*_{K,WC} = \left[1 + \left(\frac{\mathrm{Kn}}{\mathrm{St}}\right)^2 + \frac{2\mathrm{Kn}^2}{E^*\mathrm{St}^3}\right]\mathrm{erf}\left(\frac{\mathrm{St}}{1.414\mathrm{Kn}}\right) + 0.798\frac{\mathrm{Kn}}{\mathrm{St}}\exp\left[-\frac{1}{2}\left(\frac{\mathrm{St}}{\mathrm{Kn}}\right)^2\right], \tag{9a}$$

where Kn is the mass transfer or diffusive Knudsen number [59,60], expressed as

$$\mathrm{Kn} = \frac{(kTm_i)^{1/2}K(E/N)}{ea_p} \tag{9b}$$

with k representing Boltzmann's constant and T the ion temperature (assumed to be the background neutral temperature). In the strongly collisional limit, Khrapak *et al.* [38] then apply Eqs. (7a) and (7b), and the intermediate collisionality regime, proposing the equations

$$\alpha_K^* = \left([\alpha^*_{K,WC}]^{-\gamma} + [\alpha_1^*]^{-\gamma}\right)^{\frac{-1}{\gamma}} \qquad E^* \leqslant 1, \tag{9c}$$

$$\alpha_K^* = \left([\alpha^*_{K,WC}]^{-\gamma} + [\alpha_2^*]^{-\gamma}\right)^{\frac{-1}{\gamma}} \qquad E^* > 1, \tag{9d}$$

where γ is a tunable constant. Equations (9a) and (9b) are highly similar to harmonic average approaches successfully utilized to approximate both the drag force on aerosol particles in the intermediate collisionality regimes [61] as well as the transition regime particle-particle collision rates [62]. We remark that the collisional contribution in the weak collisional limit as discussed by Khrapak *et al.* [38] is neglected in Eqs. (9c) and (9d), mainly because the provided expression depends upon the Debye length to particle radius ratio, which is assumed infinite for the present calculations (leading to an ill-defined expression). The ratio of the Khrapak *et al.* attachment coefficient to the results from trajectory calculations can be expressed as

$$R_{\alpha 1} = \frac{\left[\left(\frac{\alpha^*_{K,WC}}{\alpha_1^*}\right)^{-\gamma} + 1\right]^{-1/\gamma}}{\exp(f[\ln(E^*), \ln(\mathrm{St}^*)])} E^* \leqslant 1, \tag{10a}$$

$$R_{\alpha 1} = \frac{\left[\left(\frac{\alpha^*_{K,WC}}{\alpha_2^*}\right)^{-\gamma} + 1\right]^{-1/\gamma}}{\exp(f[\ln(E^*), \ln(\mathrm{St}^*)])} E^* > 1. \tag{10b}$$

We examine the ion attachment coefficient ratio for a 1-μm radius particle with net charges from 10 to 3000, with pressure ranging from 0.5 to 50 Torr (66.7–6666 Pa) and field strengths E_x from 300 to 3000 V m^{-1}. Figure 9 displays plots of $R_{\alpha 1}$ for these conditions, with $\gamma = 1$ utilized, as proposed by Khrapak *et al.* [38] in comparison to particle-in-cell model results [63]. While higher in pressure than many laboratory-scale reactors used to examine dusty plasmas, this pressure range is encountered in plasma synthesis reactors [64–66] and leads to fully collisional sheath regions. Pressures in excess of 10 Torr (1333 Pa) are also examined to understand the effect of reducing Stokes number and Knudsen number on results. By construction, at low Stokes numbers (high pressures), both models converge to Eqs. (6a) and (6b), and at high Stokes numbers, they converge to a dimensionless attachment coefficient of 1.0. The major difference between the two approaches is an additional Kn dependence in Eq. (9a), which is a consequence of relaxing the assumption of high ion Mach number (compared to the neutral speed of sound or thermal speed). Evident in the figure, at low electric field strengths, trajectory equation results are in strong agreement with the equations of Khrapak *et al.* [38]. Greater deviations manifest at higher electric field strengths, particularly for highly charged particles at lower pressures. This deviation can be attributed to the need for an appropriate collisional term to be added to Eq. (9a). Deviations may also be attributable to the approximate nature of the neural network fit, which is slightly extrapolated to $E^* < 10^{-4}$ for higher charge, lower field strength calcula-

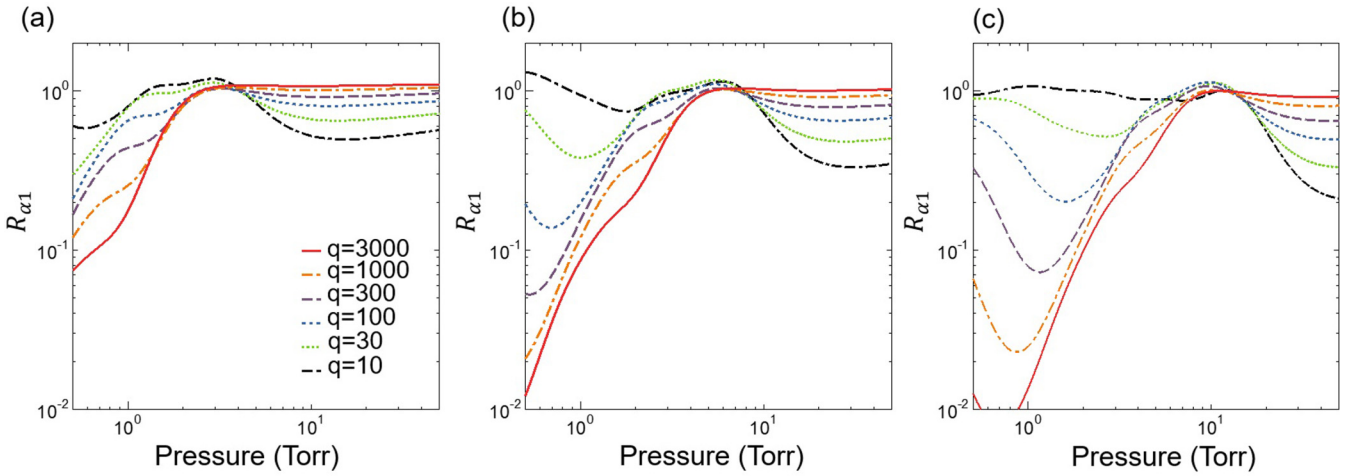

FIG. 9. Ratio of ion attachment rate coefficients for net charges from 10 to 3000 with pressure from 0.5 Torr to 50 Torr (66.7–6667 Pa) and electric field strengths E_x from 300 to 3000 V m^{-1}. $R_{\alpha 1}$ is described by Eq. (10). (a) $E = 300$ Vm^{-1}, (b) $E = 1000$ Vm^{-1}, and (c) $E = 3000$ Vm^{-1}.

tions. Acknowledging omission of a weakly collisional term and neural network imperfections, we find the two approaches agree reasonably well, with attachment coefficients within an order of magnitude of one another or better.

We next compare results to the ion attachment coefficient expression developed by Gatti and Kortshagen [25], which is applicable to ion-particle collisions within the bulk of a nonthermal plasma across a wide range of collisionality. Using the framework provided here, the ratio ($R_{\alpha 2}$) of the Gatti and Kortshagen attachment coefficient to that defined from Eq. (4) can be expressed as

$$R_{\alpha 2} = \frac{1}{\alpha_i^*}\left(\frac{1.595\mathrm{Kn}}{\mathrm{St}} + \frac{1.595}{\mathrm{Kn}E^*} + \frac{0.962}{E^*\mathrm{Kn}_R^2}\right)\exp\left(-\frac{1}{\mathrm{Kn}_R}\right) + \frac{4}{\alpha_i^* E^*}\left[1 - \left(1 + \frac{1}{\mathrm{Kn}_R}\right)\exp\left(-\frac{1}{\mathrm{Kn}_R}\right)\right], \tag{11a}$$

where Kn_R is the Gatti-Kortshagen capture radius Knudsen number, which, for large Debye length, can be expressed as

$$\mathrm{Kn}_R = 0.92\frac{E^*\mathrm{Kn}^3}{\mathrm{St}}. \tag{11b}$$

Substituting Eq. (8a) into Eq. (11a) yields

$$R_{\alpha 2} = \frac{\left(\frac{0.399\mathrm{Kn}E^*}{\mathrm{St}} + \frac{0.399}{\mathrm{Kn}} + \frac{0.241}{\mathrm{Kn}_R^2}\right)\exp\left(-\frac{1}{\mathrm{Kn}_R}\right) + \left[1 - \left(1 + \frac{1}{\mathrm{Kn}_R}\right)\exp\left(-\frac{1}{\mathrm{Kn}_R}\right)\right]}{\exp(f[\ln(E^*), \ln(\mathrm{St}^*)])} \quad E^* \leqslant 1 \tag{12a}$$

$$R_{\alpha 2} = \frac{\left(\frac{1}{E^{*2}} + \frac{2}{E^*} + 1\right)^{-1}\left(\frac{1.595\mathrm{Kn}}{\mathrm{St}} + \frac{1.595}{\mathrm{Kn}E^*} + \frac{0.962}{E^*\mathrm{Kn}_R^2}\right)\exp\left(-\frac{1}{\mathrm{Kn}_R}\right) + \left(\frac{1}{4E^*} + \frac{1}{2} + \frac{E^*}{4}\right)^{-1}\left[1 - \left(1 + \frac{1}{\mathrm{Kn}_R}\right)\exp\left(-\frac{1}{\mathrm{Kn}_R}\right)\right]}{\exp(f[\ln(E^*), \ln(\mathrm{St}^*)])} E^* > 1. \tag{12b}$$

In Fig. 10, Eq. (12) is used to examine the difference between the Gatti-Kortshagen expression and results in this study, for the same conditions as examined in Fig. 9. As pressure increases, $R_{\alpha 2}$ approaches unity for all conditions. For all charge states, at the lower field strengths examined, $R_{\alpha 2}$ is below unity, however, at the higher field strengths, $R_{\alpha 2}$ increases at lower pressures. The latter finding is a result of α_i^* decreasing sharply as the field strength increases at intermediate Stokes numbers, in the narrow but relevant range of E^* (Fig. 5). At the same time, for the cases examined, $R_{\alpha 2}$ largely remains in the 10^{-1}–10^1 range, also suggesting that the attachment coefficients derived from theories applicable to the plasma bulk and from trajectory calculations do not differ strongly from one another for microparticles in the electric field and pressure ranges examined here.

We then examine the charge on particles at steady state in Fig. 11. To compute these results, we assumed the electron attachment coefficient (α_e) is described by orbital motion limited theory, which, using the framework provided here, is expressed as

$$\alpha_e = a_p^2\left(\frac{8\pi kT_e}{m_e}\right)^{1/2}\exp\left(-\frac{\mathrm{St}}{\mathrm{Kn}^2E^*\theta_T}\right), \tag{13a}$$

where T_e is the electron temperature, θ_T is the ratio of electron temperature to ion temperature, and m_e is the electron mass. Balancing the ion current (product of ion concentration and ion attachment coefficient) and electron current (product of

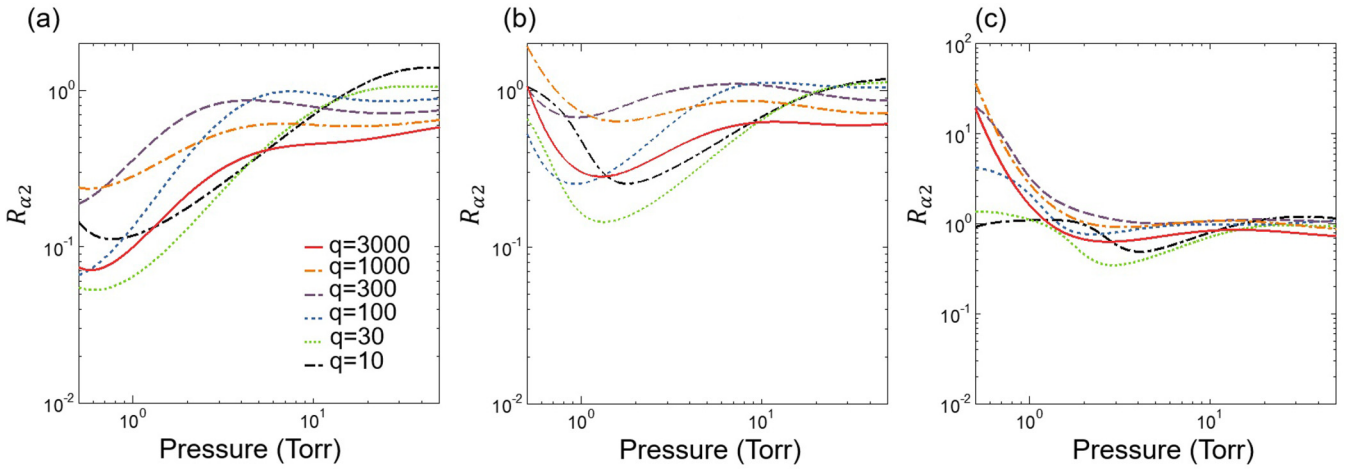

FIG. 10. Ratio of ion attachment rate coefficients for net charges from 10 to 3000 with pressure from 0.5 to 50 Torr (66.7–6667 Pa), and electric field strengths E_x from 300 to 3000 V m^{-1}. $R_{\alpha 2}$ is described by Eq. (12). (a) $E = 300$ Vm^{-1}, (b) $E = 1000$ Vm^{-1}, and (c) $E = 3000$ Vm^{-1}.

electron concentration and electron attachment coefficient) to the particle yields the equation

$$E^* = \frac{\mathrm{St}}{\mathrm{Kn}^2\theta_T \ln\left[1.595\left(\frac{\mathrm{Kn}}{\mathrm{St}}\right)\left(\frac{\theta_n\theta_T^{1/2}}{\theta_m^{1/2}}\right)\left(\frac{1}{\alpha_i^*}\right)\right]}, \tag{13b}$$

where θ_n is the ratio of electron to ion density and θ_m is the ratio of electron to ion mass. Considering a sheath region wherein $\theta_n = 0.25$, the electron temperature (T_e) is 2 eV, $T = 300$ K, and argon is the background gas, Fig. 11(a) is a contour plot of $1/E^*$ as a function of Kn and St, determined through an iterative solution to Eq. (13b) (necessary as α_i^* depends on St and E^*). $1/E^*$ is a dimensionless representation of the particle charge level. Lines of constant $1/E^*$ approximately align with lines of constant $\mathrm{Kn}^2/\mathrm{St}$ (or Kn/Ma), which follows from inspection of Eq. (13b); the dimensionless charge level decreases with increasing Stokes number and increases with increasing Knudsen number. The resulting steady-state charge on 1 μm particles is plotted in Fig. 11(b). We find that beyond 1 Torr (133 Pa), the charge level increases with increasing pressure, as the dimensional ion attachment rate decreases with increasing pressure. At high pressure, the charge level additionally decreases with increasing field strength E_x. Interestingly, at the two higher field strengths examined, we find that there is a minimum in the charge level in the 1–2 Torr (133–266 Pa) range.

In conjunction with examining charge levels, the developed equations can be used to evaluate the conditions required for particle trapping due to a balance between electrostatic forces, gravitational forces, and ion drag forces, assuming for the present test that the ion drag force is solely due to the ion collection force. At the top and bottom electrodes of a capacitively coupled parallel plate reactor, this force balance can be expressed as

$$\pi n_i m_i K^2 \left(\frac{E}{N}\right) E_x^2 a_p^2 F_i^* - qeE_x \mp \frac{4}{3}\pi\gamma a_p^3 = 0, \tag{14a}$$

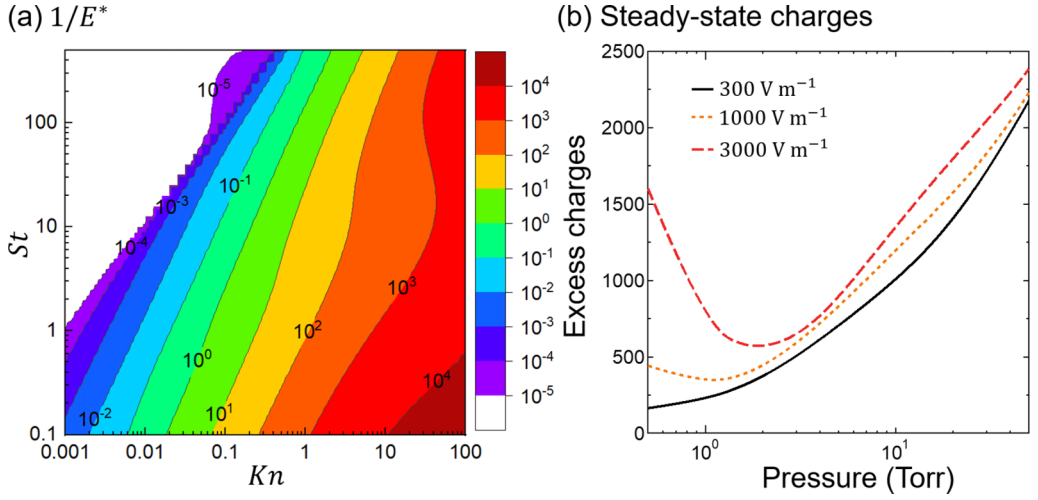

FIG. 11. The calculated $1/E^*$ value as a function of ion Stokes number St and Knudsen number Kn (a) as well as the steady-state surface charge from a collision rate balance as a function of pressure from 0.5 to 50 Torr (66.7–6667 Pa), and fields strengths E_x from 300 to 3000 V m^{-1} for a 1-μm-radius particle in argon at 300 K, with an electron temperature of 2 eV and an electron to ion density ratio of 0.25 (b).

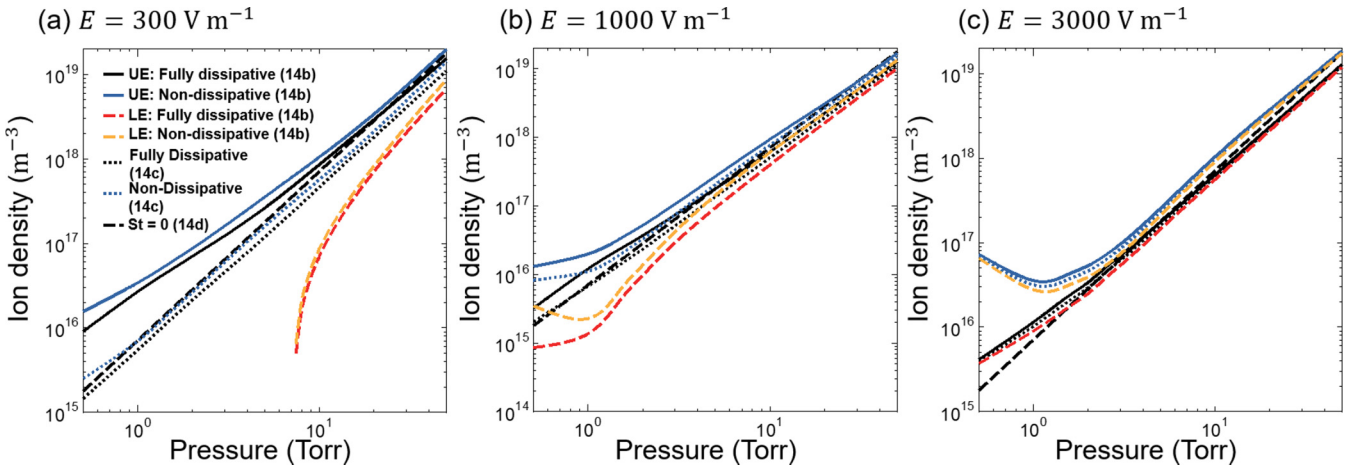

FIG. 12. Ion densities required for particle trapping predicted from Eqs. (14b)–(14d) as a function of pressure (in the 0.5–50-Torr range, or 66.7–6667-Pa range) for a 1-μm-radius particle in argon at 300 K, with an electron temperature of 2 eV and an electron to ion density ratio of 0.25. Ion drag calculation in fully dissipative and nondissipative limits is considered. UE: upper electrode. LE: lower electrode. (a) $E = 300$ Vm^{-1}, (b) $E = 1000$ Vm^{-1}, and (c) $E = 3000$ Vm^{-1}.

where γ is the specific gravity of the particle. The gravitational term and electrostatic term act in the same direction at the upper electrode and in opposite directions at the bottom electrode. Rearrangement of Eq. (14a) yields

$$n_i = \frac{\left(\frac{q}{\pi a_p^3} \pm \frac{4\gamma}{3eE_x}\right)}{\mathrm{St}F_i^*}. \tag{14b}$$

In the limit where the ratio $\frac{4\pi\gamma a_p^3}{3qeE_x}$ is small, Eq. (14b) can be further simplified to

$$n_i = \frac{q}{\pi a_p^3 \mathrm{St}F_i^*}. \tag{14c}$$

With 10^4 charges on a 1-μm particle, $\frac{4\pi\gamma a_p^3}{3qeE_x} = 0.051$ for $\gamma = 9.81 \times 10^3$ N m^{-3} and $E_x = 5 \times 10^2$ V m^{-1}, hence for highly charged particles, Eq. (14c) can be applied to link the charge level, Stokes number, dimensionless ion drag force, particle size, and ion density. In the fully dissipative low Stokes number and small field limit, Eq. (14c) additionally yields

$$n_i = \frac{3\varepsilon_0}{4K^2\left(\frac{E}{N}\right)m_i}. \tag{14d}$$

Equation (14d) suggests that for sufficiently highly charged particles (small E^*), with small Stokes numbers, and when gravitational effects are negligible, all particles, independent of particle size, will be trapped at a specific location where ion density reaches a critical value governed by the ion properties (and not the field strength). Figure 12 displays plots of the ion densities required for particle trapping close to the electrodes calculated via Eq. (13b) for specific gravity of 9.81×10^3N m^{-3} and the conditions examined in Fig. 11, along with Eqs. (14c) and (14d) calculated ion densities. This leads to a gravitational force of 0.011 pN, 0.052 pN, and 0.337 pN for field strengths of 3×10^2, 10^3, and 3×10^3 V m^{-1}, respectively, at 1 Torr (133 Pa). The ion densities plotted lead to a complete balance with these forces. We remark that these calculations represent a minimum ion density in order for balance, as the ion orbiting force is not considered in these calculations. Results are reported for the nondissipative ($F_i^* = \alpha_i^*$) and fully dissipative limits, and results with Eq. (14b) are shown for both the top and bottom electrode of a parallel plate system. The agreement between (14b) and (14c) predictions under most conditions, along with the aforementioned example calculations, shows that gravitational forces minimally influence microparticle trapping. Furthermore, while Eq. (14d) predictions are shifted from the less simplified curves, they reveal the same scaling between pressure and requisite ion density and are within an order of magnitude of Eq. (14b) for the fully dissipative limit. Correspondingly, in nearly all instances, we find that the ion density required for trapping increases approximately with the square of the pressure; this suggests that ion collection facilitated trapping is more likely at reduced pressures. Meanwhile, the electric field minimally affects the conditions required for trapping.

Finally, the minimum ion density required for trapping deviates noticeably between the fully dissipative and nondissipative predictions. This points to the need to further clarify test models of ion collection forces in future work. Nonetheless, both the fully dissipative and nondissipative ion collection force models suggest that at pressures near and below 10^0 Torr, ion densities in sheath regions are strong enough for particle trapping at both the upper and lower electrodes in parallel-plate reactors, with lower ion densities typically required in the nondissipative limit. Meanwhile, trapping requires much higher ion concentrations at increased pressure; examination of trapping at such ion densities would require consideration of screening effects (finite Debye length), and hence calculations beyond those presented here.

IV. CONCLUSIONS

Based on the performed trajectory calculations, we make the following concluding remarks:

(1) In the presence of a constant external field, ion motion about a charged particle can be parametrized at intermediate collisionality through the ion Stokes number and dimensionless field strength. We find that increasing Stokes number decreases the dimensionless ion attachment coefficients, and ion drag forces relative to the fully collisional (St = 0) limit, with the largest influence on the attachment coefficient.

(2) At intermediate Stokes number (10^0–10^2), we observe ion trajectories, including finite spirals and with a strong sensitivity to impact parameter, with resulting discontinuities in collision angle versus impact parameter curves. Such observations appear to be unique for Coulombically attracting collision partners in an intermediate collisionality regime and have been observed in prior examinations of ion trajectories about particles in dusty plasmas [20,31] as well as trajectory calculations to examine ion-ion recombination at intermediate collisionality [59], and charged dust grains in shear flows [42] with finite Stokes number. Intermediate collisionality, Coulombically attracting objects are encountered in a diverse array of systems, from the plasma sheath conditions examined in this study to fluidized beds [67], aerosol-cloud interactions [36], and atmospheric ions [68]. While trajectory calculations typically serve as a key tool to examine collisions, there has been limited prior effort to develop a unified approach to understand mass, momentum, and energy transfer rates in such systems in terms of appropriately defined dimensionless ratios. We assert that expressing rate coefficients as functions of the Knudsen number (defined differently for different processes and inversely proportionality to the dimensionless collisionality referred to elsewhere [38]) and Stokes number will find applicability in parametrizing a variety of other systems beyond particle-ion collisions.

(3) The relationships provided for the dimensionless transport rates can be coupled with models of the field strength, ion densities, and electron densities in the plasma sheath region to predict the charge distributions and forces on particles in the sheath region of parallel plate capacitively coupled plasma reactors. The developed equations suggest that ion collection forces are sufficiently strong in the sheath region to balance with electrostatic forces and trap particles, provided the ion density is at a critical value. The ion density required for trapping is strongly dependent on the system pressure, but less so on electric field strength and particle size. At the same time, future studies will need to better clarify the applicability of nondissipative and fully dissipative models of ion momentum transfer to particles at intermediate collisionality.

ACKNOWLEDGMENT

This work was supported by the Army Research Office under MURI Grant No. W911NF-18-1-0240.

APPENDIX: ION TRAJECTORY CALCULATIONS

The basic Störmer-Verlet method is applied to determine ion trajectories with the initial ion location of $x_1^* = 10\,000$, initial ion velocity $v_{1,x}^* = -1$, and time step $d\tau = (\frac{2\times10^4}{x^{*2}+y^{*2}} + 0.1)^{-1}$. By applying our nondimensional equations, we obtain the following for the initial type step:

$$\mathrm{x}_2^* = x_1^* + v_{1,\,x}^* d\tau + \frac{1}{2\mathrm{St}}\left(-1 - \frac{x_1^*}{E^*\left(x_1^{*2} + y_1^{*2}\right)^{3/2}} - \frac{1}{f\left(\frac{E}{N}\right)} v_{1,x}^*\right) d\tau^2, \tag{A1}$$

$$\mathrm{y}_2^* = y_1^* + v_{1,\,y}^* d\tau + \frac{1}{2\mathrm{St}}\left(-1 - \frac{y_1^*}{E^*\left(x_1^{*2} + y_1^{*2}\right)^{3/2}} - \frac{1}{f\left(\frac{E}{N}\right)} v_{1,y}^*\right) d\tau^2. \tag{A2}$$

Subsequently, ions are moved according to the equations

$$x_{n+2}^* = 2x_{n+1}^* - x_n^* + \frac{1}{\mathrm{St}}\left(-1 - \frac{x_{n+1}^*}{E^*\left({x_{n+1}^*}^2 + {y_{n+1}^*}^2\right)^{3/2}} - \frac{1}{f\left(\frac{E}{N}\right)} v_{n+1,x}^*\right) d\tau^2, \tag{A3}$$

$$y_{n+2}^* = 2y_{n+1}^* - y_n^* + \frac{1}{\mathrm{St}}\left(-1 - \frac{y_{n+1}^*}{E^*\left({x_{n+1}^*}^2 + {y_{n+1}^*}^2\right)^{3/2}} - \frac{1}{f\left(\frac{E}{N}\right)} v_{n+1,y}^*\right) d\tau^2. \tag{A4}$$

The ion velocity at each time is then evaluated as

$$v_{n+1,x}^* = \frac{x_{n+1}^* - x_n^*}{d\tau}, \tag{A5}$$

$$v_{n+1,y}^* = \frac{y_{n+1}^* - y_n^*}{d\tau}. \tag{A6}$$

[1] J. K. Olthoff, R. J. Vanbrunt, and S. B. Radovanov, J. Res. Natl. Inst. Stand. Technol. **100**, 383 (1995).

[2] L. J. Overzet and M. B. Hopkins, Appl. Phys. Lett. **63**, 2484 (1993).

[3] D. P. Lymberopoulos and D. J. Economou, J. Vac. Sci. Technol. A **12**, 1229 (1994).

[4] G. S. Selwyn, J. E. Heidenreich, and K. L. Haller, Appl. Phys. Lett. **57**, 1876 (1990).

[5] R. N. Carlile, S. Geha, J. F. O'Hanlon, and J. C. Stewart, Appl. Phys. Lett. **59**, 1167 (1991).

[6] H. H. Hwang and M. J. Kushner, Appl. Phys. Lett. **68**, 3716 (1996).

[7] H. H. Hwang, E. R. Keiter, and M. J. Kushner, J. Vac. Sci. Technol. A **16**, 2454 (1998).

[8] H. Setyawan, M. Shimada, and K. Okuyama, J. Appl. Phys. **92**, 5525 (2002).

[9] H. Setyawan, M. Shimada, Y. Hayashi, K. Okuyama, and S. Winardi, J. Appl. Phys. **97**, 043306 (2005).

[10] S. J. Choi, P. L. G. Ventzek, R. J. Hoekstra, and M. J. Kushner, Plasma Sources Sci. Technol. **3**, 418 (1994).

[11] G. Praburam and J. Goree, J. Vac. Sci. Technol. A **12**, 3137 (1994).

[12] A. Douglass, V. Land, K. Qiao, L. Matthews, and T. Hyde, Phys. Plasmas **19**, 013707 (2012).

[13] E. R. Keiter and M. J. Kushner, J. Appl. Phys. **83**, 5670 (1998).

[14] I. H. Hutchinson, Plasma Phys. Control. Fusion **48**, 185 (2006).

[15] J. E. Daugherty, R. K. Porteous, and D. B. Graves, J. Appl. Phys. **73**, 1617 (1993).

[16] M. Schwabe and D. B. Graves, Phys. Rev. E **88**, 023101 (2013).

[17] T. J. Sommerer, M. S. Barnes, J. H. Keller, M. J. McCaughey, and M. J. Kushner, Appl. Phys. Lett. **59**, 638 (1991).

[18] D. Samsonov and J. Goree, Phys. Rev. E **59**, 1047 (1999).

[19] S. A. Khrapak, A. V. Ivlev, G. E. Morfill, and H. M. Thomas, Phys. Rev. E **66**, 046414 (2002).

[20] S. J. Choi and M. J. Kushner, IEEE Trans. Plasma Sci. **22**, 138 (1994).

[21] J. E. Allen, Phys. Scr. **45**, 497 (1992).

[22] J. Goree, Plasma Sources Sci. Technol. **3**, 400 (1994).

[23] S. A. Khrapak and G. E. Morfill, Phys. Plasmas **15**, 114503 (2008).

[24] S. A. Khrapak, S. V. Ratynskaia, A. V. Zobnin, A. D. Usachev, V. V. Yaroshenko, M. H. Thoma, M. Kretschmer, H. Höfner, G. E. Morfill, O. F. Petrov, and V. E. Fortov, Phys. Rev. E **72**, 016406 (2005).

[25] M. Gatti and U. Kortshagen, Phys. Rev. E **78**, 046402 (2008).

[26] I. H. Hutchinson, Plasma Phys. Control. Fusion **47**, 71 (2005).

[27] I. H. Hutchinson and C. B. Haakonsen, Phys. Plasmas **20**, 083701 (2013).

[28] A. V. Ivlev, S. K. Zhdanov, S. A. Khrapak, and G. E. Morfill, Plasma Phys. Control. Fusion **46**, B267 (2004).

[29] M. D. Kilgore, J. E. Daugherty, R. K. Porteous, and D. B. Graves, J. Appl. Phys. **73**, 7195 (1993).

[30] J. E. Daugherty and D. B. Graves, J. Appl. Phys. **78**, 2279 (1995).

[31] S. J. Choi and M. J. Kushner, Appl. Phys. Lett. **62**, 2197 (1993).

[32] S. J. Choi and M. J. Kushner, J. Appl. Phys. **75**, 3351 (1994).

[33] S. A. Khrapak, A. V. Ivlev, S. K. Zhdanov, and G. E. Morfill, Phys. Plasmas **12**, 042308 (2005).

[34] I. Denysenko, K. Ostrikov, and N. A. Azarenkov, Phys. Plasmas **16**, 113707 (2009).

[35] I. H. Hutchinson, Plasma Phys. Control. Fusion **55**, 115014 (2013).

[36] A. Dépée, P. Lemaitre, T. Gelain, A. Mathieu, M. Monier, and A. Flossmann, J. Aerosol Sci. **135**, 1 (2019).

[37] K. Adamiak, A. Jaworek, and A. Krupa, IEEE Trans. Ind. Appl. **37**, 743 (2001).

[38] S. A. Khrapak, M. H. Thoma, M. Chaudhuri, G. E. Morfill, A. V. Zobnin, A. D. Usachev, O. F. Petrov, and V. E. Fortov, Phys. Rev. E **87**, 063109 (2013).

[39] H. W. Ellis, R. Y. Pai, E. W. McDaniel, E. A. Mason, and L. A. Viehland, At. Data Nucl. Data Tables **17**, 177 (1976).

[40] M. A. Lieberman and A. J. Lichtenberg, *Principles of Plasma Discharges and Materials Processing* (Wiley, New York, 1994).

[41] K. S. Friedlander, *Smoke, Dust, And Haze Fundamentals of Aerosol Dynamics (Topics In Chemical Engineering)*, 2nd ed. (Oxford University Press, New York, 2000).

[42] H. Yang and C. J. Hogan, Phys. Rev. E **96**, 032911 (2017).

[43] E. A. Mason and E. W. McDaniel, *Transport Properties of Ions in Gases* (Wiley, New York, 1988).

[44] G. J. Lindquist, D. Y. H. Pui, and C. J. Hogan, J. Aerosol Sci. **74**, 42 (2014).

[45] T. Thajudeen, B. Hunt, and C. J. Hogan, Aerosol Sci. Technol. **48**, 886 (2014).

[46] S. A. Khrapak, B. A. Klumov, and G. E. Morfill, Phys. Plasmas **14**, 034502 (2007).

[47] I. H. Hutchinson, Phys. Plasmas **14**, 074701 (2007).

[48] L. Patacchini and I. H. Hutchinson, Phys. Rev. Lett. **101**, 025001 (2008).

[49] D. Rapp and W. E. Francis, J. Chem. Phys. **37**, 2631 (1962).

[50] R. Hegerberg, T. Stefansson, and M. T. Elford, J. Phys. B At. Mol. Phys. **11**, 133 (1978).

[51] M. S. Barnes, J. H. Keller, J. C. Forster, J. A. O'Neill, and D. K. Coultas, Phys. Rev. Lett. **68**, 313 (1992).

[52] E. Goudeli, J. Lee, and C. J. Hogan, J. Aerosol Sci. **146**, 105558 (2020).

[53] A. Okabe, in *International Encyclopedia of Geography: People, the Earth, Environment and Technology* (Wiley, Oxford, 2017), Vol. 15, pp. 1–11.

[54] J. Duchon, in *Constructive Theory of Functions of Several Variables*, edited by W. Schempp and K. Zeller, Lecture Notes in Mathematics, Vol. 571 (Springer, Berlin, Heidelberg, 1977), pp. 85–100.

[55] P. Langevin, Ann. Chim. Phys. **28**, 433 (1903).

[56] J. C. Maxwell, *A Treatise on Electricity and Magnetism* (Clarendon Press, Oxford, 1873).

[57] L. Patacchini and I. H. Hutchinson, AIP Conf. Proc. **1041**, 297 (2008).

[58] J. J. Moré, in *Numerical Analysis*, edited by G. A. Watson, Lecture Notes in Mathematics, Vol. 630 (Springer, Berlin, Heidelberg, 1977), pp. 105–116.

[59] T. Tamadate, H. Higashi, T. Seto, and C. J. Hogan, J. Chem. Phys. **152**, 094306 (2020).

[60] R. Gopalakrishnan, T. Thajudeen, and C. J. Hogan, J. Chem. Phys. **135**, 054302 (2011).

[61] B. K. Annis, A. P. Malinauskas, and E. A. Mason, J. Aerosol Sci. **3**, 55 (1972).

[62] R. Gopalakrishnan and C. J. Hogan, Aerosol Sci. Technol. **45**, 1499 (2011).

[63] C. B. Haakonsen and I. H. Hutchinson, AIP Conf. Proc. **1397**, 269 (2011).

[64] E. Thimsen, U. R. Kortshagen, and E. S. Aydil, J. Phys. D: Appl. Phys. **48**, 314004 (2015).

[65] U. R. Kortshagen, R. M. Sankaran, R. N. Pereira, S. L. Girshick, J. J. Wu, and E. S. Aydil, Chem. Rev. **116**, 11061 (2016).

[66] N. J. Kramer, R. J. Anthony, M. Mamunuru, E. S. Aydil, and U. R. Kortshagen, J. Phys. D: Appl. Phys. **47**, 075202 (2014).

[67] J. Kolehmainen, A. Ozel, C. M. Boyce, and S. Sundaresan, AIChE J. **63**, 1872 (2017).

[68] A. Franchin, S. Ehrhart, J. Leppä, T. Nieminen, S. Gagné, S. Schobesberger, D. Wimmer, J. Duplissy, F. Riccobono, E. M. Dunne, L. Rondo, A. Downard, F. Bianchi, A. Kupc, G. Tsagkogeorgas, K. Lehtipalo, H. E. Manninen, J. Almeida, A. Amorim, P. E. Wagner *et al.*, Atmos. Chem. Phys. **15**, 7203 (2015).

Correction: The previously published Figures 11 and 12 contained calculation errors and have been revised, as have corresponding values and passages in text.